## Title

Divalent Cation Dependence Enhances Dopamine Aptamer Biosensing.



## Journal

ACS Applied Materials and Interfaces, 13(8)

## Authors

Nakatsuka, Nako
Abendroth, John
Yang, Kyung-Ae
et al.

## Publication Date

2021-03-03

## DOI

10.1021/acsami.0c17535

Peer reviewed

HHS Public Access

Author manuscript

*ACS Appl Mater Interfaces*. Author manuscript; available in PMC 2022 March 03.

Published in final edited form as:

*ACS Appl Mater Interfaces*. 2021 March 03; 13(8): 9425–9435. doi:10.1021/acsami.0c17535.

# Divalent Cation Dependence Enhances Dopamine Aptamer Biosensing

**Nako Nakatsuka**[1,2], **John M. Abendroth**[1,2], **Kyung-Ae Yang**[3], **Anne M. Andrews**[1,2,4,*]

[1]Department of Chemistry and Biochemistry, University of California, Los Angeles, Los Angeles, CA 90095, United States

[2]California NanoSystems Institute, University of California, Los Angeles, Los Angeles, CA 90095, United States

[3]Division of Experimental Therapeutics, Department of Medicine, Columbia University, New York, New York 10032, United States

[4]Department of Psychiatry and Biobehavioral Sciences, Semel Institute for Neuroscience and Human Behavior, and Hatos Center for Neuropharmacology, University of California, Los Angeles, Los Angeles, CA 90095, United States

## Abstract

Oligonucleotide receptors (aptamers), which change conformation upon target recognition, enable electronic biosensing under high ionic strength conditions when coupled to field-effect transistors (FETs). Because highly negatively charged aptamer backbones are influenced by ion content and concentration, biosensor performance and target sensitivities were evaluated under application conditions. For a recently identified dopamine aptamer, physiological concentrations of $Mg^{2+}$ and $Ca^{2+}$ in artificial cerebrospinal fluid produced marked potentiation of dopamine-FET-sensor responses. Divalent cation-associated signal amplification was not observed for FET sensors functionalized with a recently identified serotonin aptamer or a previously reported dopamine aptamer. Circular dichroism spectroscopy revealed $Mg^{2+}$- and $Ca^{2+}$-induced changes in target-associated secondary structure for the new dopamine aptamer but not the serotonin aptamer or the old dopamine aptamer. Thioflavin T (ThT) displacement corroborated the $Mg^{2+}$ dependence of the new dopamine aptamer for target detection. These findings imply allosteric binding interactions between divalent cations and dopamine for the new dopamine aptamer. Developing and testing

[*]**Corresponding Author**: aandrews@mednet.ucla.edu.

Author Contributions

All authors designed the experiments. NN, JMA, and KAY carried out the experiments. All authors analyzed the data, interpreted the results, and wrote the manuscript.

ASSOCIATED CONTENT

Supporting Information

The Supporting Information is available free of charge on the ACS Publications website at DOI: 10.1021/acsami.0c17535 transfer curves for dopamine and serotonin aptamer FETs in PBS; circular dichroism spectroscopy for divalent cation dependence for dopamine aptamers isolated in 1997 and 2018; thioflavin T concentration dependence of the dopamine and serotonin aptamers in the presence and absence of $MgCl_2$; table of aptamer sequences.

CONFLICTS OF INTEREST

Stem-loop receptor-based field effector sensor devices for sensing at physiological salt concentration. Co-inventors: A. M. Andrews, P. S. Weiss, N. Nakatsuka, M. N. Stojanović, and K. A. Yang, nonprovisional U.S. and foreign patents filed 2019. PCT/US2019/046891.

sensors in ionic environments that reflect intended applications are best practices for identifying aptamer candidates with favorable attributes and elucidating sensing mechanisms.

## Graphical Abstract

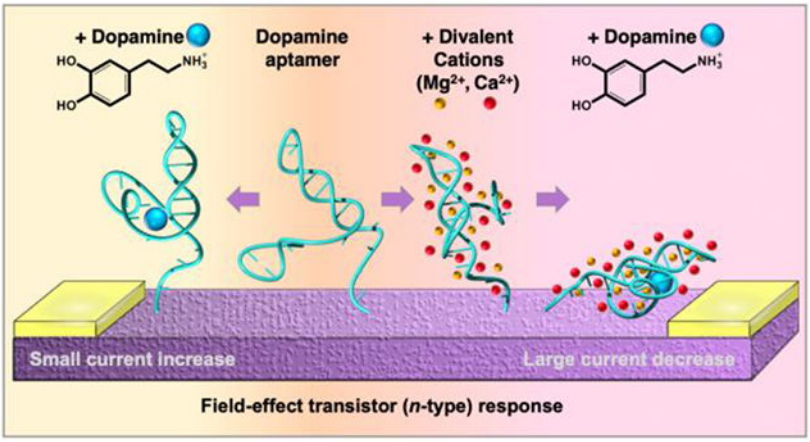


### Keywords

Oligonucleotides; $Mg^{2+}$; $Ca^{2+}$; field-effect transistor; Debye length; neurotransmitter; serotonin; circular dichroism spectroscopy

## INTRODUCTION

We have developed a generalizable strategy for small-molecule sensing under high ionic-strength conditions (*e.g.*, physiological applications, waste water, food safety).[1] We couple thin-film $In_2O_3$ FETs[2] with small DNA-based receptors, or aptamers,[3] isolated *via* solution-phase selection for target recognition (Fig. 1a).[4,5] Aptamer-functionalized FET sensors are being investigated for direct electronic target detection in clinical diagnostic, point-of-care, wearable sensor, and *in vivo* applications.[1,6,7] Understanding aptamer-target interactions in complex media and at semiconductor interfaces, particularly for FET sensing, is paramount to designing sensors with optimized detection capabilities.

Biosensing with FETs occurs by electrostatic gating of semiconducting channels upon target recognition to produce changes in source-drain transconductance (Fig. 1b).[8] The direction of change in source-drain currents depends on the semiconductor doping (*n- vs. p*-type), the band bending regime (*i.e.*, accumulation, depletion, inversion; Fig. 1c),[9] and for aptamers, the net or dominant direction of target-induced reorientation of oligonucleotides and associated solution ions.[1] Aptamers selected for target-induced stem closure are particularly advantageous for FET sensing under high-ionic strength conditions. Conformational rearrangement of highly negatively charged oligonucleotide backbones, especially stem regions,[10] produced by target association occurs in close proximity to semiconductor surfaces. Aptamer-modulated charge redistribution produces surface electric fields that alter the resistance to electron or hole flow through the semiconductor. Effective semiconductor

gating occurs even for low molecular weight targets having little or no charge and at low target concentrations (*e.g.*, femtomolar).[1]

Sensing in dilute buffers[11] or water[12,13] is inadequate for evaluating FET performance for eventual use under high ionic strength conditions. The Debye length, defined as the distance wherein reorganization of mobile charge carriers fully affects an electric field at a semiconductor surface, is inversely proportional to the square root of the ionic strength. As such, Debye screening increases rapidly with increasing ionic strength. Dilute environments do not approximate physiologically relevant (high ionic strength) conditions where detection needs to occur in close proximity, *i.e.*, nanometers, to FET surfaces.[14] Furthermore, low ion concentrations reduce the stability of secondary structures and binding conformations of highly charged biological recognition elements, altering molecular recognition.[15,16] Sensing in deionized water lacking counterions impedes highly negatively charged oligonucleotides, including aptamers, from adopting native conformations.[17]

Developing high resolution electrochemical, optical, or electronic sensors for investigating dopamine and serotonin neurotransmission is an area of intense current interest.[18–21] We recently reported novel aptamer-FET sensors for serotonin or dopamine with the ultimate goal of detecting these neurotransmitters in the brain extracellular space and other tissue environments.[1] Unlike phosphate-buffered saline (PBS), which is often used as a buffer for biosensor evaluation,[22,23] cerebrospinal fluid (CSF), the central nervous system extracellular fluid, contains millimolar concentrations of $Mg^{2+}$ and $Ca^{2+}$ (Table 1).[24] We tested serotonin- and dopamine-aptamer-FETs in artificial CSF (aCSF), which mimics the ionic content of the central nervous system extracellular milieu. We investigated the effects of $Mg^{2+}$ and $Ca^{2+}$ on aptamer-FET sensing, where an order-of-magnitude signal enhancement in the presence of the divalent cations was discovered for a high affinity dopamine aptamer but not for a high affinity serotonin aptamer, both of which we recently reported.[1]

## RESULTS AND DISCUSSION

Dopamine and serotonin aptamer-FETs were fabricated and functionalized as previously described[1,6,21] and as per the Methods section. Aptamer sequences are shown in Table S1. We initially determined sensor responses in undiluted PBS (see Figs. 2A and S5 in Nakatsuka et al. 2018; PBS was as shown in Table 1).[1] For dopamine- and serotonin-aptamer-FETs, maximal calibrated responses were ~7 ± 0.5 mV and ~14 ± 0.7 mV, respectively in PBS.[1] We had also investigated a previously reported dopamine aptamer[25] coupled to FETs.[21] The latter aptamer (dissociation constant, $K_D$=700 nM) was unable to transduce measurable FET signals in undiluted PBS. However, maximal sensor responses (~8 ± 0.4 mV)[21] in dilute (0.1×) PBS were comparable to those for the recently reported dopamine aptamer ($K_D$=150 nM) on FETs in undiluted PBS.

To approximate conditions in the brain for *in vivo* applications, we also investigated the recently identified dopamine and serotonin aptamers on FETs in aCSF to determine responses to a range of dopamine or serotonin concentrations (Fig. 2a,b). Each sensor detected its target within the physiologically relevant range found in the brain extracellular space, *i.e.*, dopamine (1 nM-1 μM)[26] and serotonin (100 pM-100 nM).[27,28] However,

whereas serotonin-aptamer FET responses were similar in PBS and aCSF,[1] the recently reported dopamine aptamer coupled to FETs showed a ten-fold greater maximal calibrated response in aCSF (~150 ± 15 mV, Fig. 2a) compared to the response in PBS (~7 ± 0.5 mV).[1] Variations in FET responses under different buffer conditions were unexpected since both of the recently reported aptamers were isolated under the same conditions, *i.e.,* PBS with 2 mM $MgCl_2$.[1]

The effects of aCSF on calibrated response magnitudes for dopamine- and serotonin-aptamer-FETs led us to consider differences between the two physiological buffers (Table 1). Both have pH values of 7.4, similar ionic strengths (*i.e.*, ~160 mM), and thus, Debye lengths (*i.e.*, ~0.7 nm). While PBS is buffered by phosphate, bicarbonate and phosphate are used in aCSF. Bicarbonate offsets rapid increases in $CO_2$ in the brain associated with neural activity and high $O_2$ consumption by producing carbonic acid. Notably, aCSF but not PBS contains $Mg^{2+}$ and $Ca^{2+}$, both of which occur at ~1.0 mM in the brain extracellular space.[24,29] Divalent cations have greater electrostatic interactions and higher degrees of hydration energy compared to monovalent ions, which affect cooperative and competitive effects of counterions in solution.[30]

To investigate the contributions of the divalent cations to FET sensing, we compared calibrated responses for different concentrations of dopamine or serotonin in aCSF with *vs.* without $Mg^{2+}$ and $Ca^{2+}$. In aCSF *sans* divalent cations, the overall ionic strength was held constant by increasing the NaCl concentration. Maximal dopamine-aptamer FET responses were greatly reduced in aCSF in the absence of $Mg^{2+}$ and $Ca^{2+}$ to ~20 ± 0.5 mV (Fig. 2a) and were only slightly higher than responses in PBS.[1] By contrast, serotonin aptamer-FETs showed comparable target-related responses in aCSF with *vs.* without divalent cations (~15 ± 0.7 mV, Fig. 2b). The response magnitudes were similar to the responses of the serotonin-aptamer-FETs in PBS.[1] The signal to noise ratios for the dopamine and serotonin aptamers were similar in aCSF with or without $Mg^{2+}$ and $Ca^{2+}$ (Table S2).

We next added increasing concentrations of $Mg^{2+}$ and $Ca^{2+}$ (500 nM-5.0 mM) to dopamine aptamer-FETs exposed to dopamine (100 μM in aCSF *sans* $Mg^{2+}$ and $Ca^{2+}$) and investigated sensor responses (Fig. 2c). Responses were maximal at 1.0 mM $Mg^{2+}$, $Ca^{2+}$, or their combination, roughly equivalent to the concentrations of the divalent cations in CSF. Addition of $Mg^{2+}$ or $Ca^{2+}$ alone produced smaller magnitude signal potentiation compared to their combination. Nevertheless, maximal sensor responses to the combination of $Mg^{2+}$ and $Ca^{2+}$ were significantly lower when the divalent cations were added *after* target exposure compared to when divalent cations were included in aCSF prior to the addition of dopamine (~20 ± 1.3 mV in Fig. 2c *vs.* ~150 ± 15 mV in Fig. 2a, respectively). This observation led us to consider that the divalent cations might impact target-induced aptamer conformational rearrangement in aCSF. Also, for the experiments in Fig. 2c, sensors were not exposed to the lower dopamine concentrations prior to a saturating dopamine concentration, which might have affected sensor response magnitudes.

Differences in dopamine sensor calibrated responses associated with divalent cations were apparent in the slopes of the concentration-dependent responses and the absolute magnitude changes in the maximal current responses (Fig. 2a). Differences in slope suggest that the

dopamine aptamer exhibits different target binding affinities ($K_D$) in the absence *vs.* presence of divalent cations. The calculated $K_D$ values differed by an order of magnitude (10 pM *vs.* 1 pM, respectively). The 10-fold differences in the response magnitudes suggest that $Mg^{2+}$ and $Ca^{2+}$ influence the structure of the dopamine aptamer-target complex (Fig. 1b). The ability of $Mg^{2+}$ to promote aptamer-target binding was corroborated in recently published work investigating target-specific folding of this dopamine aptamer.[31] Thus, we hypothesize that different aptamer conformational changes occur upon dopamine binding in the presence *vs.* absence of the divalent cations to produce different changes in surface charge rearrangement in FET semiconducting channels.

Calibrated FET responses are normalized current changes at a single gate potential selected to minimize variations between voltage sweeps (see Fig. S1 for details on calibrated response calculations).[1,32] To gain information about target-induced aptamer conformation changes, we examined non-normalized source-drain currents ($I_{DS}$) across the gate-voltage sweeps (*i.e.*, transfer curves) in a region of large target-related change (*i.e.*, 50-100 mV). The information gleaned from the transfer curves for individual FET devices is the direction of current change upon aptamer-target binding. Electron depletion or accumulation characteristics (Fig. 1c) are based on surface charge rearrangement associated with the predominant target-induced aptamer conformational reorientation. Device-to-device variations in sensor properties, such as turn-on voltage, threshold voltage, and transconductance, are normalized by calibrated response calculations.[1,32] While variations in absolute current are evident in the non-normalized transfer curves, the directions of target-related current change from baseline are consistent across devices under the same conditions.

For dopamine aptamer-FETs, $I_{DS}$ transfer curves decreased with increasing dopamine concentrations in aCSF in Figure 3a, which depicts data for a representative device.[1] The direction of change for the concentration-dependent curves indicates that target binding induces aptamer reorientation towards the semiconductor surface (Fig 1b,c).[1] Notably, for the dopamine aptamer, the transfer curve direction of change *reversed* when the divalent cations were omitted from aCSF (Fig. 3b) compared to aCSF with divalent cations (Fig. 3a). The direction of change for dopamine-aptamer association in aCSF without divalent cations was the same as the direction of change for dopamine-aptamer association in PBS (Fig. S2a). The fact that the direction of target-related transfer curves reverses supports the hypothesis that the dopamine aptamer adopts different target-associated conformations in the presence *vs.* absence of divalent cations.

Whereas dopamine aptamer-FET transfer curves decreased in response to increasing dopamine concentrations, serotonin aptamer-FET transfer curves *increased* in response to increasing serotonin concentrations in aCSF (Fig. 3c) indicating target-induced aptamer reorientation away from the semiconductor surface (Fig. 1b,c).[1] For serotonin, the direction of change of the transfer curves was *unaltered* in aCSF lacking $Mg^{2+}$ and $Ca^{2+}$ (Fig. 3d), and was similar in direction for serotonin-aptamer association on FETs in PBS (Fig. S2b).

We carried out circular dichroism (CD) spectroscopy to gain insights into aptamer secondary structural rearrangements upon target recognition under different ionic conditions.[33,34] The

sigmoidal shape of the CD spectra for oligonucleotides within the range of *ca.* 220 to 300 nm arises from the Cotton effect;[35] differential absorption changes sign at the point of maximum absorbance near 260 nm. Because the spectral positions and intensities of the negative and positive bands are sensitive to the extent of base stacking and dipole coupling, changes in CD spectra can be used to infer common secondary structural motifs that arise upon target binding to aptamers.[36]

We previously found that aptamer interaction with dopamine in aCSF containing $Mg^{2+}$ and $Ca^{2+}$ induces a blue shift in the negative CD band from 245 nm to 240 nm with increased peak intensity (ellipticity, $\theta$) (Fig. 4a). The positive CD band also undergoes a blue shift from 275 nm to 260 nm with a 2-fold increase in $\theta$. Empirical interpretation of these spectral changes indicated target-mediated parallel G-quadruplex-like formation in aCSF.[37] The structures of G-quadruplexes are determined by component strand orientation, the conformation of glycosidic bonds, and loop topology, which can be influenced by cationic coordination.[38] The polarities of parallel G-quadruplex component strands become oriented in the same direction upon target association.

Here, we focused CD studies on divalent cation effects. In the absence of dopamine, small red shifts were observed when comparing the effects of regular aCSF *vs.* aCSF *sans* $Mg^{2+}$ and $Ca^{2+}$ on the dopamine aptamer (Fig. 4b). These findings suggest that the free dopamine aptamer adopts a slightly modified divalent-cation-dependent secondary structure. However, compared to the large CD spectral changes for dopamine-aptamer association in aCSF with $Mg^{2+}$ and $Ca^{2+}$, we observed only a small blueshift in the positive band for dopamine-aptamer association in aCSF without $Mg^{2+}$ and $Ca^{2+}$ (Fig. 4a). The CD spectra for the dopamine-bound aptamer were similar regardless of whether the divalent cations were present individually or in combination, suggesting that $Mg^{2+}$ and $Ca^{2+}$ substitute for one another, at least as far as target-induced secondary structure is concerned (Fig. S3). Taken together with the FET sensing results, the dopamine aptamer CD spectral findings indicate that $Mg^{2+}$ and $Ca^{2+}$ predominantly influence the dopamine aptamer secondary structure in the target-associated state.

Regarding the recently reported serotonin aptamer, we previously found that recognition of serotonin in aCSF containing $Mg^{2+}$ and $Ca^{2+}$ produces red shifts in the negative and positive bands, as well as increases in the peak intensities (Fig. 4c).[1] The increase in $\theta$ at 215 nm, and the red shifts in the negative band from 250 nm to 260 nm and the positive band from 280 nm to 290 nm suggested that upon target recognition, the serotonin aptamer adopts an antiparallel G-quadruplex-like structure.[39,40] For antiparallel G-quadruplexes, two component strands have opposite polarities with respect to the two adjacent strands.[37]

Here, focusing on the effects of the divalent cations, we found that in the absence of serotonin, the negative and positive CD bands were slightly blue shifted in aCSF without $Mg^{2+}$ and $Ca^{2+}$ (Fig. 4d). Similar to the dopamine aptamer, these small shifts indicate that divalent cations have a minor influence on the native secondary structure of the unbound serotonin aptamer. However, unlike the new dopamine aptamer, there were negligible differences in the CD spectra of the target-bound serotonin aptamer in the presence *vs.*

absence of divalent cations, suggesting a lack of allosteric divalent cation binding effects (Fig. 4c).

An older dopamine aptamer originally reported by Mannironi *et al.* as an RNA sequence had been isolated in 50 mM Tris-HCl containing 5 mM $MgCl_2$ and 500 mM NaCl (pH 7.4).[41] The DNA homolog of this aptamer was investigated by Walsh and DeRosa under the same buffer conditions.[25] Here, we used CD spectroscopy to study this previously reported dopamine aptamer further. We observed negligible spectral changes upon exposure to dopamine or alteration of divalent cation content (Fig. S4). Prior reports have suggested that this older dopamine aptamer does not undergo substantial target-induced conformational rearrangement, which has limited its use in electrochemical aptamer sensing with redox reporters.[42]

Aptamer-target associated changes detected *via* CD spectral shifts are limited to conformational rearrangements that substantially alter oligonucleotide secondary structural motifs. Consequently, target-mediated reorganization of preformed DNA domains, including single- or double-stranded regions, stem loops, G-quartets, and/or helices do not result in CD spectral shifts.[1] Thus, some types of conformational rearrangement may be influenced by divalent cation interactions with aptamers and their targets but would not be evident by CD spectroscopy.

In addition to CD and FET transfer curves, we previously investigated target-induced changes in aptamer conformation using surface-enhanced Raman spectroscopy and Förster resonance energy transfer (FRET).[1] For two aptamers (serotonin and glucose), where we made FRET sensors, the FRET data corroborated the FET findings in terms of hypotheses about target-related directions of reorientation relative to semi-conductor surfaces. Recent work by Liu *et al.* reported on a FRET sensor for our dopamine aptamer.[31] The direction of target-related aptamer reorientation in PBS+2 mM $Mg^{2+}$ described by these authors is the same as that inferred by our FET transfer curves in aCSF. Finally, another recent paper on our serotonin aptamer found that when functioning as an electrochemical sensor,[43] the direction of aptamer reorientation upon association with serotonin is the same as we infer from transfer curves and our FRET sensor. Thus, all available data to date suggest that the directions of change of the FET transfer curves faithfully report on target-associated aptamer reorientation with respect to semiconductor surfaces.

Nonetheless, the evidence in hand points to divalent-cation-dependent effects on the recently identified dopamine aptamer but not the serotonin aptamer. Both of these aptamers were isolated from oligonucleotide libraries immobilized *via* a complementary strand, which was linked to a solid support matrix.[1] Target in solution, in this case PBS with 2 mM $MgCl_2$, drives displacement of immobilized aptamer sequences due to conformational rearrangements that favor target *vs.* complementary strand binding and aptamer stem closure. The selection library designs and strategies used to identify the adaptive-binding dopamine and serotonin aptamers investigated herein are described in detail in the supporting information for the paper where we initially reported these sequences.[1] The solution-based approach used to isolate these aptamers differs from more common methods of aptamer selection, particularly for larger protein targets, where targets are immobilized on

the solid support matrix to capture aptamer sequences from solution. Since targets are not immobilized for the solution selection strategy, all target functional groups are available for molecular recognition. This is particularly advantageous for small-molecule targets where size and restricted numbers of functional groups limit opportunities for noncovalent interactions with biomolecule binding partners.[44–46]

Since substrate effects, such as restricted diffusion and surface electric fields might impact aptamer-small-molecule interactions on FETs, we examined target interactions in solution for the recently identified aptamers to investigate whether the $Mg^{2+}$-dependent FET signal enhancement for the dopamine aptamer depends on aptamer tethering to a solid surface (*i.e.*, FET semiconducting channels) or whether divalent cation binding enhancement is also observed in solution. We used a thioflavin T (ThT) dye displacement assay. The ThT binds to G-quadruplexes and G-rich sequences *vs.* other oligonucleotide secondary motifs such as single stranded regions, duplexes, and triplexes.[47,48] While ThT has a weak fluorescence emission in the unbound state, binding to G-rich oligonucleotides results in a significant increase in fluorescence intensity. Thus, ThT acts as a reporter when investigating the binding of targets to oligonucleotides, such as aptamers.[49,50] The ThT dye displacement assay was chosen over a fluorescence quenching assay, which we used previously,[1] because hybridization between an aptamer and a complementary strand needed for the latter is strongly dependent on divalent cations.

Initially, we determined ThT association with the dopamine and serotonin aptamers in the absence of their targets. In PBS with 2 mM $MgCl_2$ (the aptamer selection buffer), fluorescence increased as a function of ThT concentration indicating that the dye binds to both aptamers (Fig. S5). While ThT-associated fluorescence was slightly higher for the dopamine aptamer in the presence *vs.* absence of $Mg^{2+}$ (Fig. S5a), the differences were negligible relative to the influence of $Mg^{2+}$ on target recognition (Fig. 5a). Serotonin aptamer-dye interactions were the same at all concentrations of ThT investigated in the presence *vs.* absence of $MgCl_2$ in PBS (Fig. S5b). In short, ThT binds to both aptamers in a concentration-dependent manner regardless of the presence of $Mg^{2+}$.

Next, we investigated the ability of the targets to displace ThT from their respective aptamers. In the presence of 2 mM $Mg^{2+}$, dopamine displaced ThT (*i.e.*, ThT fluorescence decreased) in a dopamine concentration-dependent manner (Fig 5a). Dopamine displacement of ThT increased as a function of $Mg^{2+}$ concentration within a physiological range of (0.5-2 mM; Fig. 5b), similar to $Mg^{2+}$-associated effects observed on FETs (Fig. 2c). In the absence of $MgCl_2$, dopamine was unable to displace ThT bound to the dopamine aptamer (Fig. 5a). These data imply that $Mg^{2+}$ is needed for the dopamine aptamer to adopt a dopamine-binding conformation. Unlike the dopamine aptamer, ThT bound to the serotonin aptamer was displaced by serotonin regardless of the presence of $Mg^{2+}$ suggesting that $Mg^{2+}$ is not needed for the serotonin aptamer to adopt its serotonin binding conformation (Fig. 5c).

Collectively, our findings illustrate that the differential behavior observed in terms of divalent cation sensitivity between the dopamine and serotonin aptamers is inherent to these sequences and is independent of whether the aptamers are tethered to (semiconductor)

substrates or free in solution. Additional fluorescence-based strategies (*e.g.* Förster resonance energy transfer, fluorescence anisotropy, fluorescent nucleotide analogs),[51] spectroscopic methods (*e.g.* surface-enhanced Raman spectroscopy),[1,33] mutational analysis,[31] and theoretical modeling[52–54] will be useful for investigating target-induced aptamer conformational rearrangements and allosteric effects in greater detail. Moreover, the use nuclear magnetic resonance (NMR),[55] X-ray crystallography,[56] or cryogenic electron microscopy,[57] may enable the atomically resolved structures to be solved, particularly with regard to target- and divalent-cation-bound aptamer conformations.

Unlike aptamers, riboswitches are naturally evolved single-stranded RNA regions that function as regulatory elements in messenger RNA (mRNA); they bind to small molecules and in turn, trigger changes in transcription.[58,59] In bacteria, interactions between riboswitches and small-molecules is regulated by environmental cues, such as $Mg^{2+}$ concentration.[60] For example, when engulfed by macrophages, where the $Mg^{2+}$ concentration is low, bacteria sense a decrease in $Mg^{2+}$ through a riboswitch, which triggers the expression of virulence genes.[61]

Studies probing cooperativity between $Mg^{2+}$ and small-molecule targets demonstrate that the mechanisms of riboswitch conformational change are independent for divalent cations and the target.[62–64] Selective SHAPE (2' hydroxyl acylation analyzed by primer extension) probing,[65] a method for investigating RNA secondary structures, revealed that specific regions of the *S*-adenosylmethionine-I riboswitch from *T. tengcongensis* conformationally rearrange in response to the target, while distinct riboswitch motifs are dependent on $Mg^{2+}$ to adopt a final stabilized profile.[62] As such, $Mg^{2+}$ ion concentrations were shown to shift the equilibrium of the riboswitch operation.

Similarly, a guanine-sensing riboswitch from *B. subtilis* shows $Mg^{2+}$ sensitivity in the structural preorganization of the free RNA ensemble, which then drives fast and efficient target-induced RNA folding.[63] Time-resolved NMR spectroscopy elucidated variations in the kinetic rates of target binding that were dependent on the $Mg^{2+}$ concentration. When using NMR, a more pronounced $Mg^{2+}$ effect was observed for the adenine-sensing riboswitch from *B. subtilis*, where the target-free conformational state of the RNA *sans* $Mg^{2+}$ is highly heterogeneous and contains base-pairing patterns that impede target binding.[64] The riboswitch undergoes preorganization in the presence of $Mg^{2+}$ that enables target recognition by inducing the formation of the proper base-pairing interactions.

In addition to structural stabilization of the free state of single-stranded RNA, two competing mechanisms of target recognition have been reported in the presence *vs.* absence of $Mg^{2+}$.[66] Data from fluorescence titration, nuclease digestion, and isothermal titration calorimetry have suggested that without $Mg^{2+}$, a flavin mononucleotide riboswitch interacts with its anionic target *via* an induced fit mechanism where target recognition triggers conformational change.[66] Alternately, in the presence of $Mg^{2+}$, this riboswitch undergoes a conformational selection mechanism where RNA structural rearrangement precedes target binding. These two mechanisms occur *via* different conformational intermediates and with different binding rate constants.[67] Divalent cation dependence is not limited to riboswitches

—the activity of DNA-based catalysts (DNAzymes) has also been shown to be sensitive to $Mg^{2+}$ and $Ca^{2+}$.[68]

Analogous to riboswitches, allosteric binding between divalent cations and dopamine seems to occur for the recently identified dopamine aptamer. When comparing the sensing characteristics of the three small-molecule neurotransmitter-binding aptamer sequences investigated here (Table S1), all of which were selected in buffers that contained $Mg^{2}$; only the recently identified dopamine aptamer showed unusually high FET calibrated responses associated with the presence of $Mg^{2+}$ (and $Ca^{2+}$). These findings illustrate uncertainty in predicting how ionic content will influence target-bound aptamer conformations, and thus, biosensor responses. In short, we would have failed to realize the unusual characteristics of the recently identified dopamine aptamer as a possible “black swan” had we not investigated sensing in aCSF.

## CONCLUSIONS

Together, the findings support the idea that the recently identified dopamine aptamer adopts a conformation optimized for FET detection of dopamine when $Mg^{2+}$ and $Ca^{2+}$ are present. The divalent-cation-stabilized aptamer conformation appears to be different from the aptamer conformation in the absence of $Mg^{2+}$ and $Ca^{2+}$, where dopamine still binds (*n.b.* measurable FET responses to dopamine in aCSF without divalent cations), albeit with lower target affinity (*i.e.,* higher $K_D$). In the presence of the divalent cations, the dominant direction of dopamine-associated aptamer conformational change with respect to the semiconductor surface is opposite to that in their absence. The formation of a new secondary structural motif (parallel G-quadruplex-like) when dopamine associates with its aptamer is dependent upon $Mg^{2+}$ and/or $Ca^{2+}$ Finally, although $Ca^{2+}$ was not present in the aptamer selection buffer, it appears to substitute for $Mg^{2+}$. Having one or both divalent cations present prior to exposure to dopamine stabilizes a high affinity aptamer conformation.

A widely used DNA dopamine aptamer previously investigated by Walsh and DeRosa[25] is cross-reactive to norepinephrine.[21,69] In contrast, the recently isolated dopamine aptamer shows high selectivity for dopamine *vs.* norepinephrine, as well as other similarly structured metabolites.[1] The characteristics of the new dopamine aptamer make it a promising candidate for future *in vivo* deployment. Intuitive library design and aptamer selection/counter-selection, combined with fine-tuning of sensitivities upon coupling to electronic platforms, and testing in the intended sample matrix(ices) are important for identifying optimal biosensor functionality for applications with practical impact.

## METHODS

### Materials.

Materials were purchased from Sigma-Aldrich Co. (St. Louis, MO), unless noted. Oligonucleotide sequences (Table S1) with /5ThioMC6-D/ modifications were synthesized and purified by HPLC by Integrated DNA Technologies (Coralville, IA, USA). Sequences were certified by mass spectrometry and used without further modification. The SYLGARD 184 elastomer base and curing agent were purchased from Dow Corning Corporation

(Midland, MI), and used to make polydimethylsiloxane (PDMS) wells for FET testing. Deionized water (18.2 MΩ) was obtained using a Milli-Q system (Millipore, Billerica, MA).

### Aptamer-functionalized field-effect transistors.

The FETs were fabricated as previously reported[1,6,21,70] with ultrathin (~4 nm) $In_2O_3$ semiconductor films to maximize the surface-to-volume ratios of the channels. Briefly, aqueous solutions of indium (III) nitrate hydrate ($In(NO_3)_3 \cdot xH_2O$, 99.999%) were spin-coated for 30 s at 3000 rpm onto heavily doped silicon wafers with 100-nm-thick thermally grown $SiO_2$ layers (University Wafer, Boston, MA or WaferPro, San Jose, CA). Substrates were prebaked at 150 °C for 10 min followed by thermal annealing at 350 °C for 3 h. Interdigitated source and drain electrodes (composed of 80 μm width, 1500 μm length, 10 nm Ti adhesion layer, 30 nm thick Au layer) were patterned *via* photolithography and deposited by electron-beam evaporation over the $In_2O_3$ layers. Standard solid-state characterizations of as-prepared FETs demonstrated high transconductance and uniform current distributions.

To functionalize $In_2O_3$ layers with aptamer sequences, mixed layers of 3-aminopropyl)trimethoxysilane (APTMS) and trimethoxy(propyl)silane (PTMS) were deposited from the vapor-phase *via* neat solutions containing 1:9 v/v ratio of APTMS:PTMS at 40 °C for 1 h. Substrates were subsequently incubated in a 1 mM ethanolic solution of 1-dodecanethiol for 1 h to passivate Au electrodes.

After rinsing thoroughly with ethanol, FETs were immersed in 1 mM solutions of 3-maleimidobenzoic acid *N*-hydroxysuccinimide ester (MBS) dissolved in 1:9 (v/v) dimethyl sulfoxide:PBS for 30 min to enable crosslinking of amine-terminated molecules to thiol-modified aptamers. Aptamers were prepared for attachment to FET surfaces by heating for 5 min at 95 °C in nuclease-free water followed by rapid cooling in an ice bath to relax oligonucleotides into extended conformations. Substrates were rinsed with deionized water and immersed in 1 μM DNA solutions for 1 h. Substrates were rinsed again with deionized water and blown dry with $N_2$ gas.

### Electronic measurements.

Custom PDMS wells were sealed on the Si wafer substrates allowing exposure of individual FETs to physiological buffers and sequential additions of concentrated target stock solutions in identical buffer. Artificial CSF, which mimics the ion concentrations of physiological CSF, was used as the electrolyte solution with or without $Ca^{2+}$ and/or $Mg^{2+}$. The ionic composition is shown in Table 1. All aCSF solutions were of identical ionic strength and pH, with the NaCl concentration increased from 147 mM to 151 mM when compensating for the absence of the divalent cations. The increased NaCl concentration was determined using the following formula to calculate ionic strength ($I$):

$$I = \frac{1}{2}\sum c_i z_i^2$$

where $c_i$ is the molar concentration of ions and $z_i$ is the valence of the ions.

Commercially available Ag/AgCl reference electrodes from World Precision Instruments, Inc. (Sarasota, FL) were placed in the buffer solutions within the PDMS wells above FET surfaces in a liquid-/top-gate device configuration. All FET measurements were performed using a manual analytical probe station (Signatone, Gilroy, CA) equipped with a Keithley 4200A semiconductor analyzer (Tektronix, Beaverton, OR).

Source-drain current ($I_{DS}$) transfer curves were collected by sweeping the gate-bias voltage ($V_{GS}$) from 0 to 400 mV while maintaining the drain voltage ($V_D$) at 10 mV. Five consecutive sweeps were averaged for each target concentration. Calibrated responses were calculated to minimize device-to-device variation (Fig. S1). Calibration relies on a correlation between absolute sensor responses and gate dependence in liquid-gate sensing set-ups.[32] Briefly, the absolute sensor response (ΔI), which takes into account baseline subtraction, was normalized to the change in source-drain current with voltage sweep ($\Delta I_{DS}/\Delta V_G$). All calibrated responses were calculated at a gate-bias voltage of 100 mV, which gave maximal current responses with minimal sweep-to-sweep variations.

### Circular dichroism spectroscopy.

In a typical measurement, 2 μM aptamer solutions (100 μL) were prepared in aCSF with or without divalent cations ($Mg^{2+}$ and $Ca^{2+}$) but with identical ionic strength and pH. Aptamer solutions were heated *sans* targets at 95 °C for 5 min and rapidly cooled. Once at room temperature, aptamer solutions were spiked with 100 μM stock solutions of targets prepared in the same buffer as the aptamers for final equimolar concentrations of aptamer and target. Spectra were collected on a JASCO J-715 circular dichroism spectrophotometer (Oklahoma City, OK) at room temperature within 30 min following target incubation. Four scans were acquired per sample with 0.5 nm resolution, 1.0 nm bandwidth, a 4 s response time, and a 20 nm/min scan rate. Scans are averages of four instrumental scans and are representative of two replicates per condition. Scans in aCSF (*sans* divalent cations where applicable) without aptamers or targets were subtracted as background.

### Thioflavin T dye displacement assay.

These measurements were performed in the original selection buffer (Corning PBS buffer, cat no. 21-040-CV, NaCl 154 mM, $Na_2PO_4$ 5.6 mM, and $KH_2PO_4$ 1.058 mM, pH 7.3-7.5) with or without $MgCl_2$. Aptamers were first heated in assay buffer at 95 °C for 5 min and cooled to room temperature. For ThT concentration dependence experiments (Fig. S5), the ThT concentrations were varied while the aptamer concentration was held constant (final concentration, 400 nM) in PBS with 2 mM or *sans* $MgCl_2$ (Fig. S6a). The, ThT solutions were mixed with equal volumes of aptamer solution and incubated at room temperature in the dark for 40 min prior to determining fluorescence. For target displacement experiments (Fig. 5), dopamine or serotonin were included in solutions containing ThT (final concentration 4 μM) and the respective aptamer (Fig. S6b.) Measurements were conducted in triplicate in 96-well black plates using a Flexstation II microplate reader (Molecular Devices, San Jose, CA) to record ThT fluorescence spectra at excitation and emission wavelengths of 425 nm and 490 nm, respectively. To compare the degree of ThT displacement at different dopamine and $Mg^{2+}$ concentrations, relative fluorescence was

converted to dye displacement % by normalizing to the maximum ThT fluorescence intensity at each $MgCl_2$ concentration.

### Data analysis.

All data are reported in the figures and text as means ± standard errors of the means (SEMs). Data for FET calibrated responses and ThT displacement were analyzed and graphed using GraphPad Prism 8.3 (GraphPad Software Inc., San Diego, CA). For FET responses to targets, Langmuir isotherms were fit to obtain concentration-dependent calibration curves to calculate dissociation constants ($K_D$s), where the $K_D$ is the target concentration needed to achieve half-maximal binding at equilibrium.

## Supplementary Material

Refer to Web version on PubMed Central for supplementary material.

## ACKNOWLEDGMENTS

We gratefully acknowledge the NIH (DA045550) and the NSF (CCF1518715, ECCS1509794, CMMI-1636136) for support of this work, Prof. Paul S. Weiss for feedback on experiments, and Prof. Milan N. Stojanović for feedback on the manuscript. NN is currently affiliated with the Laboratory of Biosensors and Bioelectronics in the Institute of Biomedical Engineering at ETH Zürich. JMA is currently affiliated with the Department of Physics at ETH Zürich.

## REFERENCES

(1). Nakatsuka N; Yang K-A; Abendroth JM; Cheung KM; Xu X; Yang H; Zhao C; Zhu B; Rim YS; Yang Y; Weiss PS; Stojanović MN; Andrews AM Aptamer–Field-Effect Transistors Overcome Debye Length Limitations for Small-Molecule Sensing. Science 2018, 362, 319–324. [PubMed: 30190311]

(2). Meng Z; Stolz RM; Mendecki L; Mirica KA Electrically-Transduced Chemical Sensors Based on Two-Dimensional Nanomaterials. Chem. Rev 2019, 119, 478–598. [PubMed: 30604969]

(3). Ni S; Zhuo Z; Pan Y; Yu Y; Li F; Liu J; Wang L; Wu X; Li D; Wan Y; Zhang L; Yang Z; Zhang BT; Lu A; Zhang G Recent Progress in Aptamer Discoveries and Modifications for Therapeutic Applications. ACS Appl. Mater. Interfaces 2020. DOI: 10.1021/acsami.0c05750

(4). Yang K-A; Barbu M; Halim M; Pallavi P; Kim B; Kolpashchikov DM; Pecic S; Taylor S; Worgall TS; Stojanović MN Recognition and Sensing of Low-Epitope Targets *via* Ternary Complexes with Oligonucleotides and Synthetic Receptors. Nat. Chem 2014, 6, 1003–1008. [PubMed: 25343606]

(5). Yang K-A; Chun H; Zhang Y; Pecic S; Nakatsuka N; Andrews AM; Worgall TSTS; Stojanović MN High-Affinity Nucleic-Acid-Based Receptors for Steroids. ACS Chem. Biol 2017, 12, 3103–3112. [PubMed: 29083858]

(6). Cheung KM; Yang K-A; Nakatsuka N; Zhao C; Ye M; Jung ME; Yang H; Weiss PS; Stojanović MN; Andrews AM Phenylalanine Monitoring *via* Aptamer-Field-Effect Transistor Sensors. ACS Sensors 2019, 4, 3308–3317. [PubMed: 31631652]

(7). Liu Q; Zhao C; Chen M; Liu Y; Zhao Z; Wu F; Li Z; Weiss PS; Andrews AM; Zhou C Flexible Multiplexed $In_2O_3$ Nanoribbon Aptamer-Field-Effect Transistors for Biosensing. iScience 2020, 23, 101469. [PubMed: 33083757]

(8). Pachauri V; Ingebrandt S Biologically Sensitive Field-Effect Transistors: From ISFETs to NanoFETs. Essays Biochem. 2016, 60, 81–90. [PubMed: 27365038]

(9). Weiss PS; Trevor PL; Cardillo MJ Gas-Surface Interactions on InP Monitored by Changes in Substrate Electronic Properties. J. Chem. Phys 1989, 90, 5146–5153.

(10). Bissonnette S; Del Grosso E; Simon AJ; Plaxco KW; Ricci F; Vallée-Bélisle A Optimizing the Specificity Window of Biomolecular Receptors Using Structure-Switching and Allostery. ACS Sensors 2020, 5, 1937–1942. [PubMed: 32297508]

(11). Rahim Ruslinda A; Tanabe K; Ibori S; Wang X; Kawarada H Effects of Diamond-FET-Based RNA Aptamer Sensing for Detection of Real Sample of HIV-1 Tat Protein. Biosens. Bioelectron 2013, 40, 277–282. [PubMed: 22975093]

(12). Hagen JA; Kim SN; Bayraktaroglu B; Leedy K; Chávez JL; Kelley-Loughnane N; Naik RR; Stone MO Biofunctionalized Zinc Oxide Field Effect Transistors for Selective Sensing of Riboflavin with Current Modulation. Sensors 2011, 11, 6645–6655. [PubMed: 22163977]

(13). Li Z; Rajendran B; Kamins TI; Li X; Chen Y; Williams RS Silicon Nanowires for Sequence-Specific DNA Sensing: Device Fabrication and Simulation. Appl. Phys. A Mater. Sci. Process 2005, 80, 1257–1263.

(14). Stern E; Wagner R; Sigworth FJ; Breaker R; Fahmy TM; Reed MA Importance of the Debye Screening Length on Nanowire Field Effect Transistor Sensors. Nano Lett 2007, 7, 3405–3409. [PubMed: 17914853]

(15). Lloret N; Frederiksen RS; Møller TC; Rieben NI; Upadhyay S; De Vico L; Jensen JH; Nygård J; Martinez KL Effects of Buffer Composition and Dilution on Nanowire Field-Effect Biosensors. Nanotechnology 2013, 24, 1–9.

(16). Hianik T; Ostatná V; Sonlajtnerova M; Grman I Influence of Ionic Strength, pH and Aptamer Configuration for Binding Affinity to Thrombin. Bioelectrochemistry 2007, 70, 127–133. [PubMed: 16725379]

(17). Špringer T; Šípová H; Vaisocherová H; Štepánek J; Homola J Shielding Effect of Monovalent and Divalent Cations on Solid-Phase DNA Hybridization: Surface Plasmon Resonance Biosensor Study. Nucleic Acids Res. 2010, 38, 7343–7351. [PubMed: 20624817]

(18). Patriarchi T; Cho JR; Merten K; Howe MW; Marley A; Xiong WH; Folk RW; Broussard GJ; Liang R; Jang MJ; Zhong H; Dombeck D; von Zastrow M; Nimmerjahn A; Gradinaru V; Williams JT; Tian L Ultrafast Neuronal Imaging of Dopamine Dynamics with Designed Genetically Encoded Sensors. Science 2018, 360, 1–8.

(19). Ko M; Mendecki L; Eagleton AM; Durbin CG; Stolz RM; Meng Z; Mirica KA Employing Conductive Metal-Organic Frameworks for Voltammetric Detection of Neurochemicals. J. Am. Chem. Soc 2020, 142, 11717–11733. [PubMed: 32155057]

(20). Jeong S; Yang D; Beyene AG; Del Bonis-O'Donnell JT; Gest AMM; Navarro N; Sun X; Landry MP High-Throughput Evolution of Near-Infrared Serotonin Nanosensors. Sci. Adv 2019, 5, 1–12.

(21). Kim J; Rim YS; Chen H; Cao HH; Nakatsuka N; Hinton HL; Zhao C; Andrews AM; Yang Y; Weiss PS Fabrication of High-Performance Ultrathin $In_2O_3$ Film Field-Effect Transistors and Biosensors Using Chemical Lift-off Lithography. ACS Nano 2015, 9, 4572–4582. [PubMed: 25798751]

(22). Afsahi S; Lerner MB; Goldstein JM; Lee J; Tang X; Bagarozzi DA; Pan D; Locascio L; Walker A; Barron F; Goldsmith BR Novel Graphene-Based Biosensor for Early Detection of Zika Virus Infection. Biosens. Bioelectron 2018, 100, 85–88. [PubMed: 28865242]

(23). Chu CH; Sarangadharan I; Regmi A; Chen YW; Hsu CP; Chang WH; Lee G. Y. G. Bin; Chyi JI; Chen CC; Shiesh SC; Lee G. Y. G. Bin; Wang YL Beyond the Debye Length in High Ionic Strength Solution: Direct Protein Detection with Field-Effect Transistors (FETs) in Human Serum. Sci. Rep 2017, 7, 1–15. [PubMed: 28127051]

(24). Takayuki Ohira RS Development of Artificial Cerebrospinal Fluid: Basic Experiments, and Phase II and III Clinical Trials. J. Neurol. Neurophysiol 2013, 4, 1–8.

(25). Walsh R; DeRosa MC Retention of Function in the DNA Homolog of the RNA Dopamine Aptamer. Biochem. Biophys. Res. Commun 2009, 388, 732–735. [PubMed: 19699181]

(26). Oh Y; Heien ML; Park C; Kang YM; Kim J; Boschen SL; Shin H; Cho HU; Blaha CD; Bennet KE; Lee HK; Jung SJ; Kim IY; Lee KH; Jang DP Tracking Tonic Dopamine Levels in Vivo Using Multiple Cyclic Square Wave Voltammetry. Biosens. Bioelectron 2018, 121, 174–182. [PubMed: 30218925]

(27). Yang H; Sampson MM; Senturk D; Andrews AM Sex- and SERT-Mediated Differences in Stimulated Serotonin Revealed by Fast Microdialysis. ACS Chem. Neurosci 2015, 6, 1487–1501. [PubMed: 26167657]

(28). Zhang J; Jaquins-Gerstl A; Nesbitt KM; Rutan SC; Michael AC; Weber SG In Vivo Monitoring of Serotonin in the Striatum of Freely Moving Rats with One Minute Temporal Resolution by Online Microdialysis-Capillary High-Performance Liquid Chromatography at Elevated Temperature and Pressure. Anal. Chem 2013, 85, 9889–9897. [PubMed: 24020786]

(29). Moghaddam B; Bunney BS Ionic Composition of Microdialysis Perfusing Solution Alters the Pharmacological Responsiveness and Basal Outflow of Striatal Dopamine. J. Neurochem 1989, 53, 652–654. [PubMed: 2568406]

(30). Adapa S; Malani A Role of Hydration Energy and Co-Ions Association on Monovalent and Divalent Cations Adsorption at Mica-Aqueous Interface. Sci. Rep 2018, 8, 1–12. [PubMed: 29311619]

(31). Liu X; Hou Y; Chen S; Liu J Controlling Dopamine Binding by the New Aptamer for a FRET-Based Biosensor. Biosens. Bioelectron 2020, 17, 1–7.

(32). Ishikawa FN; Curreli M; Chang H; Chen P; Zhang R; Cote RJ; Thompson ME; Zhou C A Calibration Method for Nanowire Biosensors to Suppress Device-to-Device Variation. ACS Nano 2009, 3, 3969–3976. [PubMed: 19921812]

(33). Neumann O; Zhang D; Tam F; Lal S; Wittung-Stafshede P; Halas NJ Direct Optical Detection of Aptamer Conformational Changes Induced by Target Molecules. Anal. Chem 2009, 81, 10002–10006. [PubMed: 19928834]

(34). Nagatoishi S; Tanaka Y; Tsumoto K Circular Dichroism Spectra Demonstrate Formation of the Thrombin-Binding DNA Aptamer G-Quadruplex under Stabilizing-Cation-Deficient Conditions. Biochem. Biophys. Res. Commun 2007, 352, 812–817. [PubMed: 17150180]

(35). Kuhn W Optial Rotatory Power. Annu. Rev. Phys. Chem 1958, 9, 417–438.

(36). Fasman GD Circular Dichroism and the Conformational Analysis of Biomolecules; Springer U.S., 1996.

(37). Masiero S; Trotta R; Pieraccini S; De Tito S; Perone R; Randazzo A; Spada GP A Non-Empirical Chromophoric Interpretation of CD Spectra of DNA G-Quadruplex Structures. Org. Biomol. Chem 2010, 8, 2683–2692. [PubMed: 20440429]

(38). Bhattacharyya D; Arachchilage GM; Basu S Metal Cations in G-Quadruplex Folding and Stability. Front. Chem 2016, 4, 1–14. [PubMed: 26835446]

(39). Vorlíčková M; Kejnovská I; Sagi J; Renčiuk D; Bednářová K; Motlová J; Kypr J Circular Dichroism and Guanine Quadruplexes. Methods 2012, 57, 64–75. [PubMed: 22450044]

(40). Karsisiotis AI; Hessari NMA; Novellino E; Spada GP; Randazzo A; Webba Da Silva M Topological Characterization of Nucleic Acid G-Quadruplexes by UV Absorption and Circular Dichroism. Angew. Chemie - Int. Ed 2011, 50, 10645–10648.

(41). Mannironi C; Di Nardo A; Fruscoloni P; Tocchini-Valentini GP In Vitro Selection of Dopamine RNA Ligands. Biochemistry 1997, 36, 9726–9734. [PubMed: 9245404]

(42). Farjami E; Campos R; Nielsen JS; Gothelf KV; Kjems J; Ferapontova EE RNA Aptamer-Based Electrochemical Biosensor for Selective and Label-Free Analysis of Dopamine. Anal. Chem 2013, 85, 121–128. [PubMed: 23210972]

(43). Geng X; Zhang M; Long H; Hu Z; Zhao B; Feng L; Du J A Reusable Neurotransmitter Aptasensor for the Sensitive Detection of Serotonin. Anal. Chim. Acta 2020. DOI: 10.1016/j.aca.2020.11.010

(44). Vaish A; Shuster MJ; Cheunkar S; Singh YS; Weiss PS; Andrews AM Native Serotonin Membrane Receptors Recognize 5-Hydroxytryptophan-Functionalized Substrates: Enabling Small-Molecule Recognition. ACS Chem. Neurosci 2010, 1, 495–504. [PubMed: 22778841]

(45). Cao HH; Nakatsuka N; Deshayes S; Abendroth JM; Yang H; Weiss PS; Kasko AM; Andrews AM Small-Molecule Patterning *via* Prefunctionalized Alkanethiols. Chem. Mater 2018, 30, 4017–4030. [PubMed: 30828130]

(46). Cao HH; Nakatsuka N; Liao W-S; Serino AC; Cheunkar S; Yang H; Weiss PS; Andrews AM Advancing Biocapture Substrates *via* Chemical Lift-Off Lithography. Chem. Mater 2017, 29, 6829–6839.

(47). Biancalana M; Koide S Molecular Mechanism of Thioflavin-T Binding to Amyloid Fibrils. Biochim. Biophys. Acta - Proteins Proteomics 2010, 1804, 1405–1412.

(48). De La Faverie AR; Guédin A; Bedrat A; Yatsunyk LA; Mergny JL Thioflavin T as a Fluorescence Light-up Probe for G4 Formation. Nucleic Acids Res. 2014, 42, 1–8. [PubMed: 24376271]

(49). Pei R; Stojanović MN Study of Thiazole Orange in Aptamer-Based Dye-Displacement Assays. Anal. Bioanal. Chem 2008, 390, 1093–1099. [PubMed: 18165929]

(50). Stojanović MN; Landry DW Aptamer-Based Colorimetric Probe for Cocaine. J. Am. Chem. Soc 2002, 124, 9678–9679. [PubMed: 12175205]

(51). Perez-Gonzalez C; Lafontaine DA; Penedo JC Fluorescence-Based Strategies to Investigate the Structure and Dynamics of Aptamer-Ligand Complexes. Front. Chem 2016, 4, 1–22. [PubMed: 26835446]

(52). Penna G. La; Chelli R Structural Insights into the Osteopontin-Aptamer Complex by Molecular Dynamics Simulations. Front. Chem 2018, 6, 1–11. [PubMed: 29441345]

(53). Nguyen HT; Hori N; Thirumalai D Theory and Simulations for RNA Folding in Mixtures of Monovalent and Divalent Cations. Proc. Natl. Acad. Sci. U. S. A 2019, 116, 21022–21030. [PubMed: 31570624]

(54). Jahan M; Uline MJ Quantifying $Mg^{2+}$ Binding to ssDNA Oligomers: A Self-Consistent Field Theory Study at Varying Ionic Strengths and Grafting Densities. Polymers (Basel). 2018, 10, 1–16.

(55). Bothe JR; Nikolova EN; Eichhorn CD; Chugh J; Hansen AL; Al-Hashimi HM Characterizing RNA Dynamics at Atomic Resolution Using Solution-State NMR Spectroscopy. Nat. Methods 2011, 8, 919–931. [PubMed: 22036746]

(56). Edwards AL; Garst AD; Batey RT Determining Structures of RNA Aptamers and Riboswitches by X-ray Crystallography. Methods Mol. Biol 2009, 535, 135–163. [PubMed: 19377976]

(57). Zhang K; Li S; Kappel K; Pintilie G; Su Z; Mou TC; Schmid MF; Das R; Chiu W Cryo-EM Structure of a 40 KDa SAM-IV Riboswitch RNA at 3.7 Å Resolution. Nat. Commun 2019.

(58). Nahvi A; Sudarsan N; Ebert MS; Zou X; Brown KL; Breaker RR Genetic Control by a Metabolite Binding mRNA. Chem. Biol 2002, 9, 1043–1049. [PubMed: 12323379]

(59). Roth A; Breaker RR The Structural and Functional Diversity of Metabolite-Binding Riboswitches. Annu. Rev. Biochem 2009, 78, 305–334. [PubMed: 19298181]

(60). Pontes MH; Yeom J; Groisman EA Reducing Ribosome Biosynthesis Promotes Translation during Low $Mg^{2+}$ Stress. Mol. Cell 2016, 64, 480–492. [PubMed: 27746019]

(61). García Véscovi E; Soncini FC; Groisman EA $Mg^{2+}$ as an Extracellular Signal: Environmental Regulation of Salmonella Virulence. Cell 1996, 84, 165–174. [PubMed: 8548821]

(62). Hennelly SP; Novikova IV; Sanbonmatsu KY The Expression Platform and the Aptamer: Cooperativity between $Mg^{2+}$ and Ligand in the SAM-I Riboswitch. Nucleic Acids Res. 2013, 41, 1922–1935. [PubMed: 23258703]

(63). Buck J; Wacker A; Warkentin E; Wöhnert J; Wirmer-Bartoschek J; Schwalbe H Influence of Ground-State Structure and $Mg^{2+}$ Binding on Folding Kinetics of the Guanine-Sensing Riboswitch Aptamer Domain. Nucleic Acids Res. 2011, 39, 9768–9778. [PubMed: 21890900]

(64). Noeske J; Schwalbe H; Wöhnert J Metal-Ion Binding and Metal-Ion Induced Folding of the Adenine-Sensing Riboswitch Aptamer Domain. Nucleic Acids Res. 2007, 35, 5262–5273. [PubMed: 17686787]

(65). Deigan KE; Li TW; Mathews DH; Weeks KM Accurate SHAPE-Directed RNA Structure Determination. Proc. Natl. Acad. Sci. U. S. A 2009, 106, 97–102. [PubMed: 19109441]

(66). Rode AB; Endoh T; Sugimoto N Crowding Shifts the FMN Recognition Mechanism of Riboswitch Aptamer from Conformational Selection to Induced Fit. Angew. Chemie - Int. Ed 2018, 57, 6868–6872.

(67). Vogt AD; Di Cera E Conformational Selection or Induced Fit? A Critical Appraisal of the Kinetic Mechanism. Biochemistry 2012, 51, 5894–5902. [PubMed: 22775458]

(68). Zhou W; Zhang Y; Ding J; Liu J In Vitro Selection in Serum: RNA-Cleaving DNAzymes for Measuring $Ca^{2+}$ and $Mg^{2+}$. ACS Sensors 2016, 1, 600–606.

(69). Nakatsuka N; Cao HH; Deshayes S; Melkonian AL; Kasko AM; Weiss PS; Andrews AM Aptamer Recognition of Multiplexed Small-Molecule-Functionalized Substrates. ACS Appl. Mater. Interfaces 2018, 10, 23490–23500. [PubMed: 29851335]

(70). Huang W; Zhu B; Chang SY; Zhu S; Cheng P; Hsieh YT; Meng L; Wang R; Wang C; Zhu C; McNeill C; Wang M; Yang Y High Mobility Indium Oxide Electron Transport Layer for an Efficient Charge Extraction and Optimized Nanomorphology in Organic Photovoltaics. Nano Lett 2018, 18, 5805–5811. [PubMed: 30075074]

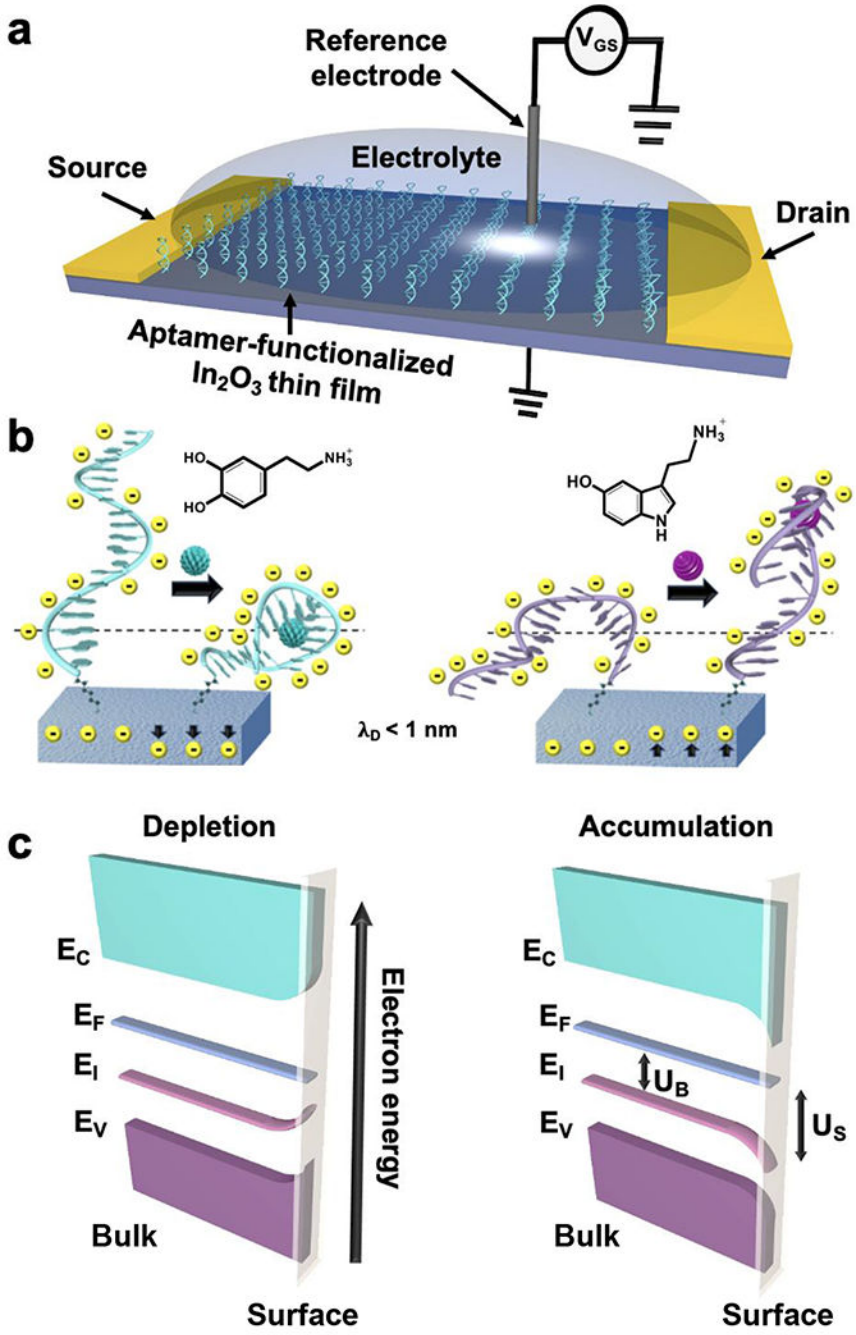


**Figure 1.**

(**a**) Schematic of aptamer-functionalized field-effect transistor operated in liquid-gate configuration. (**b**) Illustrations showing examples of two general types of conformational changes that aptamers undergo upon target recognition on *n*-type semiconducting channels. For a recently reported dopamine aptamer, dopamine binding induces negatively charged oligonucleotide backbones to reorient closer to the semiconductor surface within the Debye length ($\lambda_D$) producing electron depletion and a decrease in the current response (left). Alternately, when negatively charged serotonin aptamer backbones reorient away from a

semiconductor surface upon target binding, excess electrons accumulate in the *n*-type semiconductor producing current increases (right). (**c**) Energy level diagrams and charge distributions for an *n*-type semiconductor showing band bending at the surface for depletion (left) and accumulation (right). $E_C$: conduction band energy, $E_F$: Fermi energy, $E_I$: intrinsic energy level, $E_V$: valence band energy, $U_B$: bulk potential, $U_S$: surface potential.

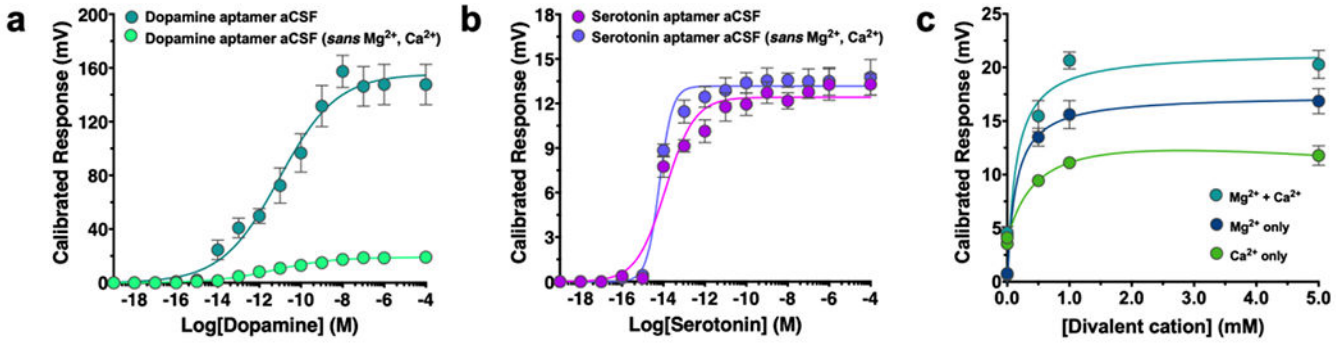


**Figure 2.**

Field-effect transistor (FET) measurements in artificial cerebrospinal fluid (aCSF). **(a)** Dopamine aptamer-FETs showed ten-fold greater calibrated responses to dopamine in the presence of divalent cations in aCSF *vs.* in their absence. **(b)** Conversely, serotonin aptamer-FETs showed comparable electronic responses in the presence *vs.* absence of divalent cations in aCSF. Data in aCSF containing $Mg^{2+}$ and $Ca^{2+}$ are reproduced from ref 1. **(c)** Effects of the addition of different concentrations of $Ca^{2+}$, $Mg^{2+}$, or both on dopamine-aptamer-FETs exposed to a saturating concentration of dopamine (100 μM) in aCSF *sans* divalent cations. Data are means ± standard errors of the means (SEMs) for $N$=6 FETs per condition in a,b, and $N$=3 FETs per condition in c. Error bars are too small to be depicted in some cases.

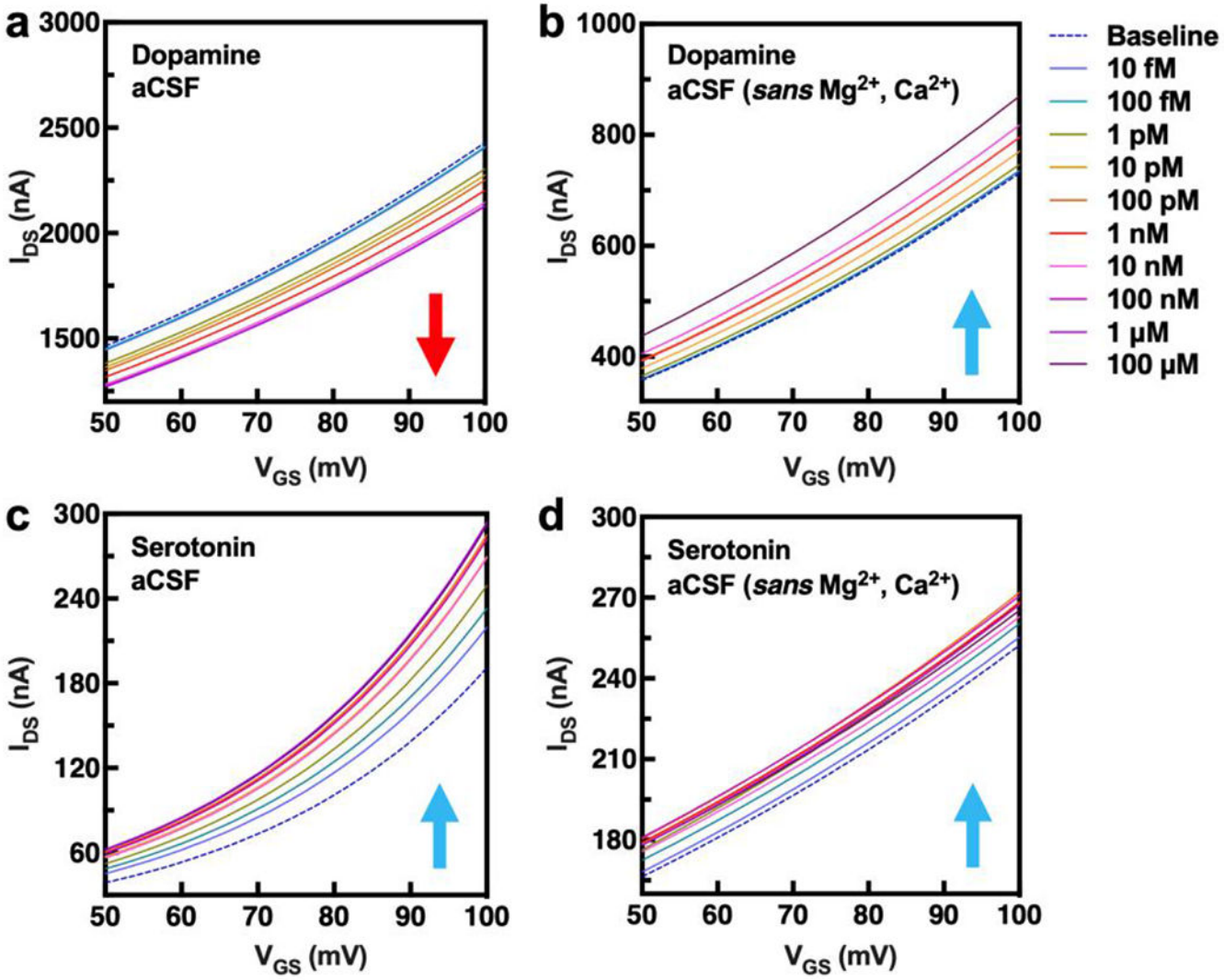


**Figure 3.**

Transfer curves for individual devices representing average behavior for gate voltage sweeps at dopamine- and serotonin-aptamer-functionalized field-effect transistors (FETs) in artificial cerebrospinal fluid (aCSF) with or without $Mg^{2+}$ and $Ca^{2+}$. **(a)** Currents decrease for dopamine-aptamer-FETs as a function of increasing dopamine concentration in aCSF (see also Fig 1a). **(b)** A reversal in the direction of change in target-related currents was observed in the absence of divalent cations in aCSF for dopamine-aptamer-FETs. **(c)** For serotonin-aptamer-FETs in aCSF, source-drain currents increased with increasing serotonin concentrations in aCSF (see also Fig. 1b). **(d)** When divalent cations were absent from aCSF, the direction of current change remained the same for serotonin-aptamer-FETs. Data in (a) and (c) are reproduced with permission from ref. 1. Copyright 2018 American Association for the Advancement of Science.

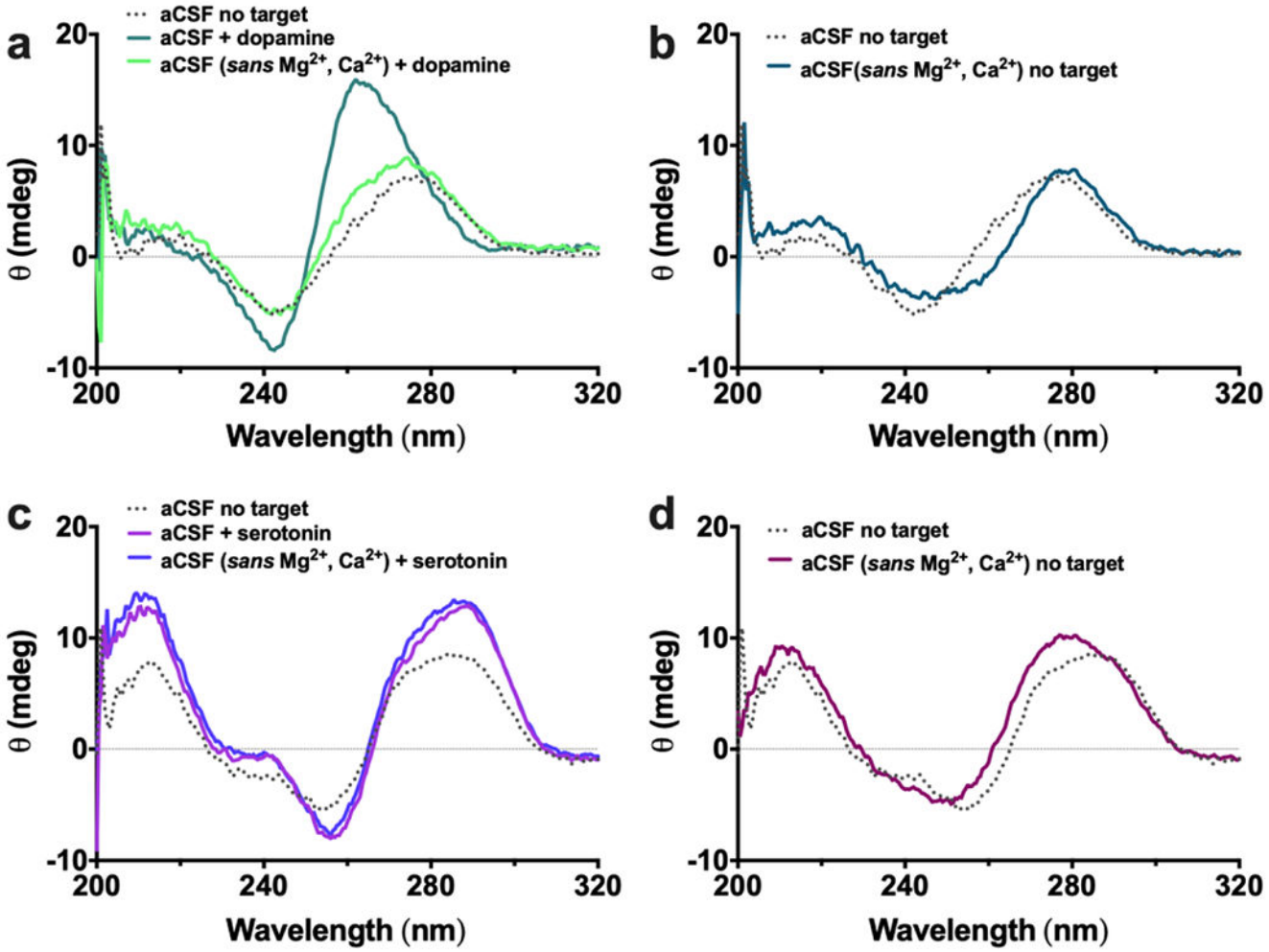


**Figure 4.**

Circular dichroism (CD) spectroscopy of dopamine and serotonin aptamers in target-bound- *vs.* unbound states and with different divalent cation content. **(a)** Representative CD spectra of the dopamine aptamer showed blue shifts (*i.e.*, shifts to shorter wavelengths) in the negative and positive bands and a large increase in peak magnitudes when equimolar dopamine was included in the artificial cerebrospinal fluid (aCSF) but only when $Mg^{2+}$ and $Ca^{2+}$ were present in aCSF. **(b)** Representative CD spectra of the unbound (free, no target) dopamine aptamer showed small red shifts for the major negative and positive bands when divalent cations were absent from aCSF indicating that $Mg^{2+}$ and $Ca^{2+}$ have a minor influence on the unbound secondary structure. **(c)** Representative CD spectra of the unbound *vs.* target-bound serotonin aptamer in aCSF. The major negative and positive peaks shifted to longer (red) wavelengths and increased in magnitude. However, the serotonin aptamer-target complex was negligibly affected when divalent cations were omitted from aCSF. **(d)** Representative CD spectra of the unbound serotonin aptamer showed small blue shifts for the major negative and positive bands when divalent cations were absent from aCSF. Spectra are representative of $N$=2 samples per condition. Data in aCSF with and without target in a-d are reproduced from ref 1.

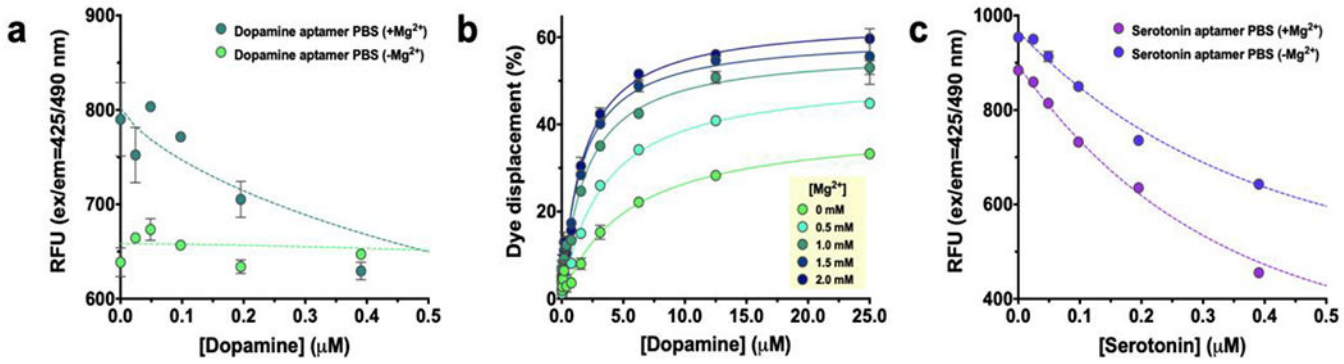


**Figure 5.**

Thioflavin T (ThT) displacement from aptamers by their targets in the presence *vs.* absence of $Mg^{2+}$. **(a)** Reductions in fluorescence intensity associated with concentration-dependent dopamine displacement of ThT binding to the dopamine aptamer only occurred in the presence of $Mg^{2+}$ (2 mM). **(b)** The displacement of ThT by dopamine increased with increasing physiologically relevant concentrations of $Mg^{2+}$. **(c)** Concentration-dependent serotonin displacement of ThT binding to the serotonin aptamer occurred regardless of the presence of $Mg^{2+}$. Data were obtained in phosphate-buffered saline and are averages of $N$=3 samples per condition ± standard errors of the means where error bars are too small to be depicted in some cases.

**Table 1.**

**(Left)** Composition of phosphate-buffered saline (PBS), which is commonly used (often in dilute concentrations) for biosensor testing. **(Right)** Artificial cerebrospinal fluid (aCSF) mimics the ionic composition of the brain extracellular space and includes millimolar concentrations of $Mg^{2+}$ and $Ca^{2}$.

| PBS | | aCSF (brain fluid) | |
|---|---|---|---|
| **Salt** | **Conc. (mM)** | **Salt** | **Conc. (mM)** |
| NaCl | 137 | NaCl | 147 |
| KCl | 2.7 | KCl | 3.5 |
| $Na_2HPO_4$ | 10 | $NaH_2PO_4$ | 1.0 |
| $KH_2PO_4$ | 1.8 | $NaHCO_3$ | 2.5 |
| | | $MgCl_2$ | 1.2 |
| | | $CaCl_2$ | 1.0 |